Subsonic gas flow in a straight and uniform microchannel

By YITSHAK ZOHAR, SYLVANUS YUK KWAN LEE,
WING YIN LEE, LINAN JIANG AND PIN TONG

Department of Mechanical Engineering, The Hong Kong University of Science and Technology,
Clear Water Bay, Kowloon, Hong Kong

A nonlinear equation based on the hydrodynamic equations is solved analytically using perturbation expansions to calculate the flow field of a steady isothermal, compressible and laminar gas flow in either a circular or a planar microchannel. The solution takes into account slip-flow effects explicitly by utilizing the classical velocity-slip boundary condition, assuming the gas properties are known. Consistent expansions provide not only the cross-stream but also the streamwise evolution of the various flow parameters of interest, such as pressure, density and Mach number. The slip-flow effect enters the solution explicitly as a zero-order correction comparable to, though smaller than, the compressible effect. The theoretical calculations are verified in an experimental study of pressure-driven gas flow in a long microchannel of sub-micron height. Standard micromachining techniques were utilized to fabricate the microchannel, with integral pressure microsensors based on the piezoresistivity principle of operation. The integrated microsystem allows accurate measurements of mass flow rates and pressure distributions along the microchannel. Nitrogen, helium and argon were used as the working fluids forced through the microchannel. The experimental results support the theoretical calculations in finding that acceleration and non-parabolic velocity profile effects were found to be negligible. A detailed error analysis is also carried out in an attempt to expose the challenges in conducting accurate measurements in microsystems.

1. Introduction

Micromachining technology has reached a mature stage as its products, Micro-Electro-Mechanical Systems (MEMS), find applications in a widening field of disciplines. MEMS applications range from consumer products to industrial tools, biomedical microdevices and instrumentation. In order to design such microsystems effectively, it is crucial to understand the physical laws governing their operation. Therefore, micromechanics in general and micro fluid mechanics in particular has become a major research field (Ho & Tai 1996).

Most microsystems will inevitably include fluid flows either in a primary or secondary role. When dealing with flow in configurations of microns or less, many unexpected phenomena have been observed (Ho & Tai 1998), such as the friction factor in microscale (Pfahler *et al.* 1991). The flows in macro- and microsystems are not quite the same. There is still a great deal of difficulty in understanding the complex surface effects, which play a major role in both liquid and gas flows in microfluidic systems. In microscale liquid flows, electrokinetic (Hunter 1981) and polar mechanic

effects (Stokes 1984) become important, while rarefaction has to be considered in gas flows. As the characteristic length scale of the system approaches the mean free path (m.f.p.), the flow cannot be modelled based on the continuum hypothesis and, thus, microscopic effects have to be taken into account. The ratio between the m.f.p. and the characteristic length scale, the Knudsen number (Kn), is used to distinguish among different flow regimes (Schaaf & Chambre 1961). The flow is considered to be in the continuum regime if $Kn < 10^{-3}$, while for $10 < Kn$ it is considered a free molecular flow. A rarefied gas flow, such as in a microchannel, can be considered neither continuous nor free molecular. A further classification is needed, i.e. slip-flow for $10^{-3} < Kn < 10^{-1}$ and transition flow for $10^{-1} < Kn < 10^{1}$, each suggesting a particular type of analysis. This classification is based on empirical information, and it is widely accepted that in the slip-flow regime the continuum model is still valid provided the velocity-slip and temperature-jump boundary conditions are utilized (Beskok & Karniadakis 1994).

Rarefied gas flow was intensively studied in the early 1960s by solving the (continuous) Boltzmann equation using semi-analytical or pure numerical methods (Cercignani, Illner & Pulvirenti 1994). However, there are some difficulties in applying the Boltzmann equation to shear flows, e.g. channel flow, and analytical solutions are obtained under highly restrictive assumptions (Chu & Zohar 2000). This approach is more suitable for the transition and free-molecular flow regimes. Numerical modelling using the direct simulation Monte Carlo method has also been conducted (Piekos & Breuer 1996). There are a few theoretical studies addressing compressible flow in straight and uniform micro-channels using continuum flow models. Prud'homme, Chapman & Bowen (1986) obtained a perturbation solution of the Navier–Stokes equations for a circular tube with the assumption of no radial pressure gradient. Van den Berg, ten Seldam & van der Gulik (1993*a*, *b*) also used perturbation expansion methods to solve the isothermal, compressible Navier–Stokes equations for laminar flow in a capillary without considering slip flow effects. They derived analytical expressions for the effects of flow acceleration and a non-parabolic velocity profile. Harley *et al.* (1995) further simplified the mathematical model to obtain a closed-form solution for the gas density distribution in a micro-channel, but still without considering slip flow effects. The Knudsen-number effect was introduced only in the estimation of the Poiseuille number. Beskok, Karniadakis & Trimmer (1996) extended the classical Maxwell/Smoluchowski slip conditions by including higher-order Knudsen-number effects in order to simulate heat and momentum transfer in gaseous microflows, and the competing effects of compressibility and rarefaction were highlighted. Arkilic, Schmidt & Breuer (1997) presented a two-dimensional analysis with a first-order velocity-slip boundary condition, demonstrating the effects of both compressibility and rarefaction in long microchannels. They showed that the zero-order analytic solution corresponded well with experimental results of Pong *et al.* (1994).

Experimental research on flows in uniform but not-straight (Lee, Wong & Zohar 2001) or in straight but non-uniform microchannels (Lee, Wong & Zohar 2002*a*, *b*) is underway. However, flow through a straight and uniform channel is the simplest and most fundamental configuration in microfluidic systems. Accordingly, flows in straight microchannels have been studied experimentally and theoretically. Although rarefied internal gas flows are encountered both in low-pressure environments and in micron-size geometries at standard atmospheric conditions, conducting experiments in such minute systems is still a formidable challenge. Sreekanth (1968) studied the flow of rarefied gases under large pressure gradients and high Knudsen numbers

(*Kn*). The experimental measurements of the friction factor agreed well with theoretical predictions assuming a single-coefficient wall slip model and locally fully developed flow, as long as $Kn < 0.13$. (Note that $Kn \sim 0.1$ is widely recognized as the boundary between the slip, $Kn < 0.1$, and the free-molecular flow regime, $Kn > 0.1$.) Choi, Barron & Warrington (1991), on the other hand, measured a friction factor 17% lower than the theoretical predictions for nitrogen flow in tubes with diameters smaller than $10\,\mu$m. Wu & Little (1983) reported friction factors larger than predictions by established correlations. They attributed the anomalous results to the high degree of surface roughness in their channels. Harley *et al.* (1995) investigated low-Reynolds-number, high-subsonic-Mach-number, compressible flow in microchannels with $Kn < 0.38$. They reported measured values of the friction constant within 8% of theoretical calculations based on isothermal, locally fully developed flow. Furthermore, they concluded that the pressure in each cross-section could be assumed uniform and the transverse velocity could be neglected. Arkilic *et al.* (1997) carried out an experimental investigation into gaseous flow with slight rarefaction through long microchannels. They compared measurements of helium mass flow rate in a $1.33\,\mu$m channel with their two-dimensional analysis of the Navier–Stokes equations incorporating a first-order velocity-slip boundary condition. The agreement between the experimental data and the calculations was well within 5%. Wu *et al.* (1998) reported that the microchannel cross-section could be enlarged under high pressure, which resulted in higher flow rates.

All the experimental results discussed so far were based on flow rate measurements only. This is not surprising since measuring flow properties in a microconfiguration is a challenging task (Ho & Tai 1998). The need for microflow diagnostics to provide more detailed information has been recognized. Liu *et al.* (1993) integrated pressure sensors to measure the pressure distributions along microchannels (Pong *et al.* 1994). Jiang *et al.* (1999) suspended micro-thermistors, $0.4\,\mu$m in thickness, across microchannels $1.4\,\mu$m in height for local temperature measurements. Meinhart, Wereley & Santiago (1999) used particle image velocimetry to map the velocity field in liquid flows through microchannels. Shih *et al.* (1996) conducted detailed measurements of both mass flow rate and pressure distribution. They found the pressure drop in microchannels to be very high, leading to significant changes in the gas density. Consequently, the pressure distribution was not linear as in typical creeping flows, and it is a useful property for examining analytical results. In this work, similar procedures are followed to measure flow rates and pressure distributions in a microchannel using nitrogen, argon and helium as the working fluids. The experimental results are used to verify the theoretical calculations. Moreover, a detailed uncertainty analysis is carried out in order to highlight the pitfalls unique to measurements in microfluidic systems, which could partially explain the somewhat conflicting data previously reported.

2. Mathematical modelling

An isothermal steady compressible pressure-driven microchannel flow is examined. The flow through a straight uniform channel is assumed to be two-dimensional, either planar or circular, and the various equations are expressed in the appropriate coordinate system; x is the streamwise (axial) coordinate, y the cross-stream (radial), and z the spanwise (azimuthal). The full hydrodynamical equations are rarely used to set up the mathematical flow model. Instead, restricted forms of these equations are

usually adapted to allow analytical solutions. The assumptions made in the present work are the following:

(i) The fluid is Newtonian.

(ii) The microchannel half-height or radius H is small compared to its length L, $H/L < 10^{-3}$, and it is also small compared to the width, $H/D < 10^{-1}$, for planar flow.

(iii) The cross-stream (radial) and spanwise (azimuthal) velocity components, v and w, can be neglected, i.e. the gas flow is strictly uni-axial and laminar. The Reynolds number is on the order of one, $Re = 2Hu_a/v \sim 1$, with u_a the average velocity and v the kinematic viscosity.

(iv) The pressure P is a function of the streamwise coordinate x only, $P = P(x)$.

(v) The flow is in the slip regime. The Knudsen number is on the order of 0.1, i.e. $Kn = \lambda/2H \sim 10^{-1}$; λ is the gas mean free path.

(vi) A slip boundary condition is utilized.

(vii) There are no gravity effects.

(viii) Both the shear, μ, and the bulk viscosity of the fluid, η, are constant in the pressure range throughout the microchannel.

(ix) The flow is two-dimensional, i.e. all spanwise (azimuthal) gradients are equal to zero.

Under these simplifying conditions, the equations of motion for gas flow in either planar or circular microchannel reduce to

$$\frac{\partial(\rho u)}{\partial x} = 0, \tag{1a}$$

$$\rho u \frac{\partial u}{\partial x} = -\frac{\partial P}{\partial x} + \mu \frac{1}{y^m} \frac{\partial}{\partial y}\left(y^m \frac{\partial u}{\partial y}\right) + \mu\left(\frac{4}{3} + \frac{\eta}{\mu}\right)\frac{\partial^2 u}{\partial x^2}, \tag{1b}$$

$$\mu\left(\frac{1}{3} + \frac{\eta}{\mu}\right)\frac{\partial^2 u}{\partial x \, \partial y} = \frac{\partial P}{\partial y} = 0, \tag{1c}$$

where ρ and u are the fluid density and streamwise velocity component, respectively. The index m is used to distinguish between axisymmetric flow, $m = 1$, and flow between two parallel plates, $m = 0$. The working fluid is assumed to be an ideal gas such that

$$P = \rho R T, \tag{2}$$

where R is the gas specific constant. Thus, if the temperature $T = $ constant and $P = P(x)$, the density also depends on x only. Integration of the continuity equation then implies

$$\rho(x)u(y, x) = G(y) \quad \text{or} \quad u(y, x) = u_c(x)F(y). \tag{3}$$

Due to the symmetry of the flow, the dimensionless velocity-profile function $F(y)$ is maximum and, thus, $\mathrm{d}F/\mathrm{d}y = 0$ at $y = 0$. $F(y = 0) = 1$ if $u_c(x)$ is the centreline velocity $u(0, x)$. A reduced velocity-profile function $E(r)$ is defined by

$$E(r) \equiv F(y) \quad \text{with} \quad r = y/H. \tag{4}$$

Substituting $u(y, x)$ in the equation of motion yields the following governing equation:

$$\rho u_c \frac{\mathrm{d}u_c}{\mathrm{d}x} E^2(r) = -\frac{\mathrm{d}P}{\mathrm{d}x} + \frac{\mu u_c}{H^2}\mathrm{f}\{E(r)\} + \mu\left(\frac{4}{3} + \frac{\eta}{\mu}\right)\frac{\mathrm{d}^2 u_c}{\mathrm{d}x^2}E(r), \tag{5}$$

with the operator f defined as

$$f \equiv \frac{1}{r^m} \frac{d}{dr} \left(r^m \frac{d}{dr} \right).$$ (6)

The centreline velocity is replaced by the density as follows:

$$u_c(x) = W / \rho(x),$$ (7)

where W is related to the mass-flow rate according to

$$Q = (2 - m) D^{1-m} (2\pi)^m \int_0^H \rho(x) u(y, x) y^m \, dy$$

$$= (2 - m)(2\pi)^m D^{1-m} (H)^{1+m} W \int_0^1 E(r) r^m \, dr.$$ (8)

Thus, W is a constant of the flow. The governing equation is then multiplied by $\rho(x)$ to obtain

$$-\frac{W^2}{\rho} \frac{d\rho}{dx} E^2(r) + \mu \left(\frac{4}{3} + \frac{\eta}{\mu} \right) W \rho \frac{d}{dx} \left(\frac{1}{\rho^2} \frac{d\rho}{dx} \right) E(r) = -\rho \frac{dP}{dx} + \frac{\mu W}{H^2} f\{E(r)\}.$$ (9)

Before it is solved, equation (9) is put into a dimensionless form. Initially the equation is further simplified by integrating it over the length of the microchannel from $x = 0$ to $x = L$; the pressure $P(x)$ decreases from $P_i = P(0)$ to $P_o = P(L)$ and the density $\rho(x)$ from $\rho_i = \rho(0)$ to $\rho_o = \rho(L)$. The result is

$$W^2 Y E^2(r) - \mu \left(\frac{4}{3} + \frac{\eta}{\mu} \right) W Z E(r) = X + \frac{\mu W L}{H^2} f\{E(r)\},$$ (10)

where the parameters X, Y and Z are defined by

$$X = \int_{P_o}^{P_i} \rho \, dP = \langle \rho(P) \rangle \Delta P, \quad Y = \ln \frac{\rho_i}{\rho_o}, \quad Z = \int_{\rho_o}^{\rho_i} \rho \, d \left(\frac{1}{\rho^2} \frac{d\rho}{dx} \right).$$ (11)

$\Delta P = P_i - P_o$ is the pressure drop across the microchannel, and $\langle \rho(P) \rangle$ is a density defined as the average of $\rho(P)$ over the pressure interval $[P_i, P_o]$. Equation (10) can now be re-written as

$$A f\{E(r)\} - B E^2(r) + C E(r) + 1 = 0,$$ (12)

where the constants A, B and C are defined as

$$A = \frac{\mu W L}{H^2 X}, \quad B = \frac{W^2 Y}{X}, \quad C = \mu \left(\frac{4}{3} + \frac{\eta}{\mu} \right) \frac{W Z}{X}.$$ (13)

Normalizing the velocity profile by the centreline velocity and taking into account the flow symmetry results in

$$E(r)|_{r=0} = 1, \quad \left. \frac{dE(r)}{dr} \right|_{r=0} = 0.$$ (14)

Assuming the accommodation coefficient to be one and neglecting second-order terms, the velocity slip boundary condition at the wall is given by (Beskok *et al.* 1996)

$$u(y, x)|_{y=H} = -\lambda(x) \left. \frac{du}{dy} \right|_{y=H} \quad \text{or} \quad u_c(x) E(r)|_{r=1} = -2Kn(x) u_c(x) \left. \frac{dE}{dr} \right|_{r=1},$$ (15)

where $Kn(x)$ is inversely proportional to the pressure $P(x)$:

$$Kn(x) \equiv \frac{\lambda(x)}{2H} = \frac{\mu}{P(x)} \left(\frac{\pi RT}{2} \right)^{1/2} \frac{1}{2H}. \tag{16}$$

Integrating equation (15) between the channel inlet and outlet allows the introduction of an average Knudsen number Kn as follows:

$$Kn = \int_0^L Kn(x) u_c(x) \, \mathrm{d}x \bigg/ \int_0^L u_c(x) \, \mathrm{d}x. \tag{17}$$

The corresponding slip boundary condition becomes

$$E(r)|_{r=1} = -2Kn \left. \frac{\mathrm{d}E(r)}{\mathrm{d}r} \right|_{r=1}. \tag{18}$$

For an incompressible fluid $\rho_i = \rho_o$, so that the parameters Y and Z and, consequently, the constants B and C are zero. Therefore, in the next section, the present flow problem is treated by a perturbation method in terms of the small parameters B and C, which are unknown in advance but depend on the solution itself.

3. Perturbation solutions

Equation (12) will be solved analytically, using a perturbation method, for compressible laminar flow either between parallel plates ($m = 0$) or in a circular capillary ($m = 1$) with the slip boundary condition, following the same approach as van den Berg *et al.* (1993*a*).

3.1. *General formalism*

The parameters B and C vanish for incompressible flow and are assumed to be small for compressible flow. Therefore, the velocity-profile function $E(r)$ is expanded in powers of these parameters as follows:

$$E^{(n)}(r) = \sum_{i=0}^n \sum_{j=0}^n E_{i,j}(r) B^i C^j, \quad i + j \leqslant n, \tag{19}$$

where the superscript (n) denotes the order n of the approximation. This power series implies

$$A^{(n)} = A^{(0)} \left[1 + \sum_{i=0}^n \sum_{j=0}^n A_{i,j} B^i C^j \right], \quad 1 \leqslant i + j \leqslant n. \tag{20}$$

These two power series expansions are then substituted into equation (12). The solution of the resulting equation is derived in successive powers of $B^i C^j$ by equating the corresponding terms on both sides of the equation up to the second order:

zero order

$$i = 0, j = 0: \quad A^{(0)} \mathrm{f}\{E_{0,0}(r)\} + 1 = 0; \tag{21}$$

first order

$$i = 1, j = 0: \quad A^{(0)}[A_{1,0} \mathrm{f}\{E_{0,0}(r)\} + \mathrm{f}\{E_{1,0}(r)\}] - E_{0,0}^2(r) = 0, \tag{22a}$$

$$i = 0, j = 1: \quad A^{(0)}[A_{0,1} \mathrm{f}\{E_{0,0}(r)\} + \mathrm{f}\{E_{0,1}(r)\}] + E_{0,0}(r) = 0; \tag{22b}$$

second order

$$i = 2, j = 0: \quad A^{(0)}[A_{2,0}f\{E_{0,0}(r)\} + A_{1,0}f\{E_{1,0}(r)\} + f\{E_{2,0}(r)\}]$$
$$- 2E_{0,0}(r)E_{1,0}(r) = 0, \tag{23a}$$

$$i = 1, j = 1: \quad A^{(0)}[A_{1,1}f\{E_{0,0}(r)\} + A_{0,1}f\{E_{1,0}(r)\} + A_{1,0}f\{E_{0,1}(r)\} + f\{E_{1,1}(r)\}]$$
$$= 2E_{0,0}(r)E_{0,1}(r) - E_{1,0}(r), \tag{23b}$$

$$i = 0, j = 2: \quad A^{(0)}[A_{0,2}f\{E_{0,0}(r)\} + A_{0,1}f\{E_{0,1}(r)\} + f\{E_{0,2}(r)\}] + E_{0,1}(r) = 0. \tag{23c}$$

These sets of equations are solved at successive order in terms of the total power of B^iC^j. The nth set consists of $n + 1$ equations; each separately contains only one unknown function $E_{i,j}(r)$ and a corresponding constant $A_{i,j}$, with $i + j = n$. The remaining functions and constants, for which $i + j < n$, have already been found from the sets of equations of the previous order. Thus, the functions $E_{i,j}(r)$ can be found, while the values of $A_{i,j}$ and the two integration constants are determined from the application of the normalization and boundary conditions:

$$E_{0,0}(r)|_{r=0} = 1 \Rightarrow E_{i,j}(r)|_{r=0} = 0 \quad \text{for} \quad i + j > 0, \tag{24a}$$

$$\left.\frac{\mathrm{d}E_{i,j}(r)}{\mathrm{d}r}\right|_{r=0} = 0 \quad \text{and} \quad E_{i,j}(r)|_{r=1} = -2Kn \left.\frac{\mathrm{d}E_{i,j}(r)}{\mathrm{d}r}\right|_{r=1} \quad \text{for} \quad i + j \geqslant 0. \tag{24b}$$

In order to find the expression for the mass flow rate at the order n, the nth-order velocity profile $E^{(n)}(r)$ is substituted into the integrand of equation (8). The mass flow rate is constant for a given flow, which leads to the following expression for $W^{(n)}$:

$$\frac{W^{(0)}}{W^{(n)}} = 1 + \sum_{i=0}^{n} \sum_{j=0}^{n} W_{i,j}B^iC^j, \quad 1 \leqslant i + j \leqslant n, \tag{25}$$

with

$$W_{i,j} = \int_0^1 E_{i,j}(r)r \, \mathrm{d}r \Big/ \int_0^1 E_{0,0}(r)r \, \mathrm{d}r, \tag{26}$$

and the mass flow rate is given by

$$Q^{(n)} = Q^{(0)} \left[1 + \sum_{i=0}^{n} \sum_{j=0}^{n} A_{i,j}B^iC^j\right] \left[1 + \sum_{i=0}^{n} \sum_{j=0}^{n} W_{i,j}B^iC^j\right], \quad 1 \leqslant i + j \leqslant n, \tag{27}$$

where, for consistency of the calculation, the final series expansion for $Q^{(n)}$ in terms of B^iC^j should be trancated to terms with $i + j \leqslant n$.

The exact values of the parameters B and C can be calculated simultaneously from the respective expressions in equation (16), which are written for that purpose as

$$B = \frac{B^{(0)}}{\left[1 + \displaystyle\sum_{i=0}^{\infty} \sum_{j=0}^{\infty} W_{i,j}B^iC^j\right]^2}, \quad C = C^{(0)} \left[1 + \sum_{i=0}^{\infty} \sum_{j=0}^{\infty} A_{i,j}B^iC^j\right], \quad 1 \leqslant i + j, \tag{28}$$

with

$$B^{(0)} = \frac{Y}{X} W^{(0)2}, \quad C^{(0)} = \mu \left(\frac{4}{3} + \frac{\eta}{\mu}\right) \frac{Z}{X} W^{(0)}. \tag{29}$$

The consistency of the perturbation calculations of B and C should be maintained

throughout each order. This will be accomplished by developing B and C into series of successive powers of $B^i C^j$ and, subsequently, by transformation of both series together into power series of the zero-order terms, restricting these series to that finite number of terms that does not exceed the order of the calculation. It is straightforward to recover the numerical results of van den Berg *et al.* (1993a) by selecting $Kn = 0$ and $m = 1$.

3.2. *Zero-order solution*

From equation (21) it follows that

$$A^{(0)}\mathrm{f}\{E_{0,0}(r)\} = -1. \tag{30}$$

Integration of this differential equation under the boundary conditions in (24) leads to

$$E^{(0)}(r) = E_{0,0}(r) = 1 - \frac{r^2}{1 + 4Kn} \quad \text{and} \quad A^{(0)} = \frac{1 + 4Kn}{2(m + 1)}. \tag{31}$$

$E_{0,0}(r)$, with $Kn = 0$, represents the well-known parabolic velocity profile. Substitution of $A^{(0)}$ into definition (13) to obtain $W^{(0)}$ allows the calculation of the leading-order mass flow rate:

$$Q^{(0)} = \frac{1 + (3 + m)2Kn}{(m + 1)^2(m + 3)}(2 - m)(2\pi)^m D^{1-m} H^{3+m} \frac{X}{\mu L} = Q_i \alpha_C (1 + \alpha_S), \tag{32}$$

where Q_i is the mass flow rate for an incompressible flow, α_C is the 'compression' factor, and α_S is the correction due to slip-flow effect. These expressions, evaluated for a plane channel ($m = 0$), are given by

$$Q_i = \frac{2}{3}\frac{DH^3}{\mu L}\Delta P\frac{P_o}{RT}, \quad \alpha_C = \frac{P_i + P_o}{2P_o} = \frac{\overline{P}}{P_o}, \quad \alpha_S = 6Kn. \tag{33}$$

Thus, the solution for $Q^{(0)}$, the mass flow rate of a compressible slip flow at zero order, formally includes corrections to the compressible- and slip-flow effects; namely these are leading-order effects.

3.3. *First-order solution*

The first-order solutions $A_{1,0}$, $E_{1,0}(r)$ and $W_{1,0}$ are computed from equation (22a) by substituting the zero-order solutions for $E_{0,0}(r)$ and $A^{(0)}$, equation (31), followed by repeated integration with application of the boundary conditions (24). For $m = 0$, this results in

$$E_{1,0}(r) = \frac{2}{(1 + 4Kn)^2}\left[\frac{240Kn^2 + 72Kn + 6}{45(1 + 4Kn)^2}r^2 - \frac{1}{6}r^4 + \frac{1}{30(1 + 4Kn)}r^6\right], \tag{34a}$$

$$A_{1,0} = \frac{-960Kn^3 - 560Kn^2 - 132Kn - 11}{15(1 + 4Kn)^3}, \tag{34b}$$

$$W_{1,0} = \frac{392Kn^2 + 90Kn + 5}{105(1 + 6Kn)(1 + 4Kn)^3}. \tag{34c}$$

Likewise, the solutions $A_{0,1}$, $E_{0,1}(r)$ and $W_{0,1}$ are computed from equation (22b). By imposing a consistency restriction on equation (28), the values of B and C are found to be

$$B = B^{(1)} = B^{(0)} \quad \text{and} \quad C = C^{(1)} = C^{(0)}. \tag{35}$$

The final form of the first-order solution for the mass flow rate is
$m = 0$:

$$\frac{Q^{(1)}}{Q^{(0)}} = 1 - \frac{840Kn^3 + 420Kn^2 + 84Kn + 6}{35(1+4Kn)^2(1+6Kn)} \frac{XYH^4}{\mu^2 L^2}$$

$$+ \frac{60Kn^2 + 20Kn + 2}{5(1+4Kn)(1+6Kn)} \left(\frac{4}{3} + \frac{\eta}{\mu}\right) \frac{ZH^2}{L}, \tag{36a}$$

$m = 1$:

$$\frac{Q^{(1)}}{Q^{(0)}} = 1 - \frac{32Kn^2 + 8Kn + 1}{32(1+4Kn)^2} \frac{XYH^4}{\mu^2 L^2} + \frac{48Kn^2 + 12Kn + 1}{6(1+4Kn)(1+8Kn)} \left(\frac{4}{3} + \frac{\eta}{\mu}\right) \frac{ZH^2}{L}. \tag{36b}$$

The mass flow rate with the first-order correction can be re-written as

$$Q^{(1)} = Q^{(0)}(1 + \alpha_{AP}) = Q_i \alpha_C (1 + \alpha_S)(1 + \alpha_{AP}), \tag{37}$$

with α_{AP} being the correction due to flow acceleration and the non-parabolic velocity profile, given for $Kn = 0$ and $m = 0$ by

$$\alpha_{AP} = -\frac{6}{35} \frac{XYH^4}{\mu^2 L^2} = -\frac{3}{35} \frac{H^4}{\mu^2 L^2} (P_i^2 - P_o^2) \ln \frac{P_i}{P_o}. \tag{38}$$

3.4. *Second-order solution*

The second-order solutions are computed from equation (23), following the same procedure as applied for the first-order solutions. For example ($m = 0$):

$$A_{2,0} = \frac{-376320Kn^4 - 182400Kn^3 - 37808Kn^2 - 3912Kn - 163}{4725(1+4Kn)^6}, \tag{39a}$$

$$E_{2,0}(r) = \frac{-2}{675(1+4Kn)^5} r^{10} + \frac{1}{35(1+4Kn)^4} r^8 + \frac{320Kn^3 - 240Kn^2 - 84Kn - 7}{225(1+4Kn)^6} r^6$$

$$- \frac{960Kn^3 + 400Kn^2 + 84Kn + 7}{45(1+4Kn)^5} r^4 + \left[\frac{3225600Kn^5 + 2472960Kn^4}{4725(1+4Kn)^7}\right.$$

$$\left. + \frac{906240Kn^3 + 179248Kn^2 + 18264Kn + 761}{4725(1+4Kn)^7}\right] r^2, \tag{39b}$$

$$W_{2,0} = \frac{12418560Kn^5 + 8785920Kn^4 + 3061344Kn^3 + 558640Kn^2 + 49200Kn + 1640}{51975(1+4Kn)^6(1+6Kn)}. \tag{39c}$$

$A_{1,1}$, $A_{0,2}$, $E_{1,1}(r)$, $E_{0,2}(r)$, $W_{1,1}$ and $W_{0,2}$ are similarly calculated. According to equation (27), the perturbation solution for the mass flow rate is then given by

$$Q^{(2)} = Q^{(0)}[1 + (A_{1,0} + W_{1,0})B + (A_{0,1} + W_{0,1})C + (A_{2,0} + A_{1,0}W_{1,0} + W_{2,0})B^2$$

$$+ (A_{0,1}W_{1,0} + A_{1,0}W_{0,1} + W_{1,1})BC + (A_{0,2} + A_{0,1}W_{0,1} + W_{0,2})C^2]. \tag{40}$$

To compute B and C in the second-order results consistently, they are re-written as

$$B = B^{(0)} \left[1 + \sum_{i=0}^{2} \sum_{j=0}^{2} B_{i,j} B^{(0)i} C^{(0)j} \right],$$

$$C = C^{(0)} \left[1 + \sum_{i=0}^{2} \sum_{j=0}^{2} C_{i,j} B^{(0)i} C^{(0)j} \right], \quad 1 \leqslant i + j \leqslant 2. \tag{41}$$

By using equation (28), where the coefficients $W_{i,j}$ and $A_{i,j}$ are known for $i, j = 0, 1, 2$, the coefficients $B_{i,j}$ and $C_{i,j}$ are found to be

$$B_{1,0} = 2A_{1,0}, \quad B_{0,1} = 2A_{0,1}, \quad B_{2,0} = 2A_{2,0} + A_{1,0}^2,$$
$$B_{1,1} = 2A_{1,1} + 2A_{0,1}A_{1,0}, \quad B_{0,2} = 2A_{0,2} + A_{0,1}^2; \tag{42a}$$
$$C_{1,0} = A_{1,0}, \quad C_{0,1} = A_{0,1}, \quad C_{2,0} = A_{2,0}, \quad C_{1,1} = A_{1,1}, \quad C_{0,2} = A_{0,2}, \tag{42b}$$

and, hence, B and C are given by

$$B = B^{(2)} = B^{(0)}(1 + B_{1,0}B^{(0)} + B_{0,1}C^{(0)} + B_{2,0}B^{(0)2} + B_{1,1}B^{(0)}C^{(0)} + B_{0,2}C^{(0)2}), \tag{43a}$$

$$C = C^{(2)} = C^{(0)}(1 + C_{1,0}B^{(0)} + C_{0,1}C^{(0)} + C_{2,0}B^{(0)2} + C_{1,1}B^{(0)}C^{(0)} + C_{0,2}C^{(0)2}). \tag{43b}$$

The second-order mass flow rate can now be calculated as follows:

$$\frac{Q^{(2)}}{Q^{(0)}} = 1 + Q_{1,0}B^{(0)} + Q_{0,1}C^{(0)} + Q_{2,0}B^{(0)2} + Q_{1,1}B^{(0)}C^{(0)} + Q_{0,2}C^{(0)2}. \tag{44}$$

3.5. *Axial-flow solution*

Consistent with the assumption that the pressure (as well as the density) is a function of the streamwise coordinate only, equation (9) can be integrated in the cross-stream direction to provide the streamwise dependence of the flow parameters, resulting in

$$\frac{B1}{\rho(\xi)} \frac{d}{d\xi} \rho(\xi) - C1\rho(\xi) \frac{d}{d\xi} \left[\frac{1}{\rho(\xi)^2} \frac{d}{d\xi} \rho(\xi) \right] = \rho(\xi) \frac{d}{d\xi} P(\xi) - A1, \tag{45}$$

where

$$A1 = (1 + m) \frac{\mu W L}{H^2} \frac{dE(r)}{dr} \bigg|_{r=1} = AX(1 + m) \frac{dE(r)}{dr} \bigg|_{r=1}, \tag{46a}$$

$$B1 = (1 + m)W^2 \int_0^1 r^m E(r)^2 \, dr = \frac{BX}{Y}(1 + m) \int_0^1 r^m E(r)^2 \, dr, \tag{46b}$$

$$C1 = (1 + m)\mu \left(\frac{4}{3} + \frac{\eta}{\mu} \right) \frac{W}{L} \int_0^1 r^m E(r) \, dr = \frac{CX}{ZL}(1 + m) \int_0^1 r^m E(r) \, dr, \tag{46c}$$

and $\xi = x/L$ is the non-dimensional streamwise coordinate. The parameters $A1$, $B1$ and $C1$ are constants in terms of the known parameters A, B and C. It is convenient to re-write the equation in terms of $\rho^2(\xi)$, while replacing the pressure P by the density ρ:

$$\frac{B1}{2\rho^2} \frac{d}{d\xi} \rho^2 - \frac{C1}{2} \left[\frac{1}{\rho^2} \frac{d^2}{d\xi^2} \rho^2 - \frac{3}{2(\rho^2)^2} \left(\frac{d}{d\xi} \rho^2 \right)^2 \right] = \frac{RT}{2} \frac{d}{d\xi} \rho^2 - A1. \tag{47}$$

The streamwise solution is expanded in powers of $B1$ and $C1$, which are also small parameters, as follows:

$$\rho^2(\xi) = \delta_0(\xi) + B1\delta_{1,0}(\xi) + C1\delta_{0,1}(\xi) + B1^2\delta_{2,0}(\xi) + B1C1\delta_{1,1}(\xi) + C1^2\delta_{0,2}(\xi). \quad (48)$$

This power series expansion is substituted into equation (47), and the solution of the resulting equation is then derived in successive powers of $B1^iC1^j$:

zero order

$$i = 0, j = 0: \quad RT\frac{\mathrm{d}}{\mathrm{d}\xi}\delta_0(\xi) = 2A1; \quad (49)$$

first order

$$i = 1, j = 0: \quad RT\frac{\mathrm{d}}{\mathrm{d}\xi}\delta_{1,0}(\xi) = \frac{1}{\delta_0(\xi)}\frac{\mathrm{d}}{\mathrm{d}\xi}\delta_0(\xi), \quad (50a)$$

$$i = 0, j = 1: \quad RT\frac{\mathrm{d}}{\mathrm{d}\xi}\delta_{0,1}(\xi) = \frac{3}{2[\delta_0(\xi)]^2}\left[\frac{\mathrm{d}}{\mathrm{d}\xi}\delta_0(\xi)\right]^2 - \frac{1}{\delta_0(\xi)}\frac{\mathrm{d}^2}{\mathrm{d}\xi^2}\delta_0(\xi), \quad (50b)$$

and similarly for the second order, i.e. $\delta_{2,0}(\xi)$, $\delta_{1,1}(\xi)$ and $\delta_{0,2}(\xi)$. Successive integrations of these differential equations between inlet ($\xi = 0$) and outlet ($\xi = 1$) provide the solutions:

$$i = 0, j = 0: \quad \delta_0(\xi) = \delta_0(1) - \frac{2A1}{RT}(1 - \xi), \quad (51a)$$

$$i = 1, j = 0: \quad \delta_{1,0}(\xi) = \frac{1}{RT}\ln\frac{\delta_0(\xi)}{\delta_0(1)}, \quad (51b)$$

$$i = 0, j = 1: \quad \delta_{0,1}(\xi) = \frac{A1}{RT}\left[\frac{3}{RT\delta_0(1)} - \frac{3}{2A1\xi - 2A1 + RT\delta_0(1)}\right], \quad (51c)$$

etc. Substitution of the solutions into equation (48) yields the following first-order solution:

$$\rho^2(\xi) = \delta_0(\xi) + \frac{B1}{RT}\ln\frac{\delta_0(\xi)}{\delta_0(1)} - \frac{C1}{(RT)^3}\frac{6A1^2}{\delta_0(1)}\frac{1-\xi}{\delta_0(\xi)}. \quad (52)$$

The parameters $A1$, $B1$ and $C1$ are calculated based on equation (46). In order to complete the solution, the parameter Z defined in equation (11) can now be evaluated ($m = 0$):

$$Z = \frac{-3X}{2LRT\delta_0(1)} + \left(6Y - \frac{5X}{RT\delta_0(1)}\right)\frac{(60Kn^2 + 20Kn + 2)W^{(0)2}}{15LRT(1+4Kn)^2\delta_0(1)}$$

$$+ \left(\frac{9}{2} + \frac{7X}{RT\delta_0(1)}\right)\frac{1+6Kn}{3+12Kn}\left(\frac{4}{3} + \frac{\eta}{\mu}\right)\frac{\mu X W^{(0)}}{[LRT\delta_0(1)]^2}. \quad (53)$$

Once the density squared is known, the streamwise dependence of both the density and the pressure is readily available. Using the relations: $Kn(x)P(x) = Kn_oP_o$ and $u_c(x)\rho(x) = W$, the average Knudsen number can now be evaluated explicitly:

$$Kn = \int_0^L Kn(x)u_c(x)\,\mathrm{d}x \bigg/ \int_0^L u_c(x)\,\mathrm{d}x = Kn_o\rho_o\int_0^1 \rho^{-2}\,\mathrm{d}\xi \bigg/ \int_0^1 \rho^{-1}\mathrm{d}\xi, \quad (54)$$

where ρ_o and Kn_o are the outlet density and Knudsen number, respectively, and substitution of $\delta_0(1) = \rho_o^2$ leads to

$$Kn \approx \frac{\sqrt{RT}Kn_o\rho_o}{2[\sqrt{RT\rho_o^2 - 2A1} - \sqrt{RT\rho_o^2}]}\ln\left(1 - \frac{2A1}{RT\rho_o^2}\right). \quad (55)$$
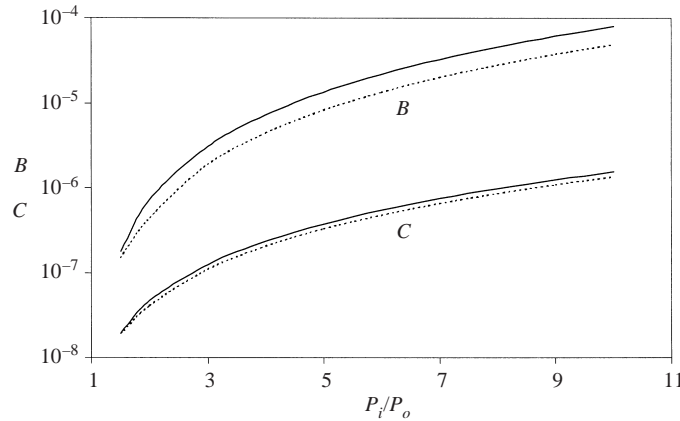
FIGURE 1. The dependence of the parameters B and C on the pressure ratio P_i/P_o:
——, $Kn = 0$; $\cdots\cdots$, $Kn = 0.05$.

4. Analytical results

The initial assumptions on which the entire analytical derivation is based, namely the magnitude and ordering of the small parameters in the expansion procedure, need to be verified. The solution was expanded in powers of B and C, since they vanish for $P_i/P_o \rightarrow 1$. Hence, the ratios B/A and C/A are calculated in figure 1 as a function of the pressure ratio. Both are smaller than 10^{-4}, demonstrating that these are indeed small parameters for the compressible flow. However, the ordering is not accurate since $C/B \sim 10^{-2}$, while it was assumed in the analysis that $C/B \sim 1$. This is not a major issue as terms on the order of C should be considered as second order like B^2, and C^2 to be fourth order like B^4. Terms of the order BC should no longer be considered second order but rather third order like B^3. This means that the contribution of the longitudinal viscosity can be neglected as assumed in many theoretical derivations. However, this ordering has no bearing on the solutions obtained.

The normalized zero-, first- and second-order solutions of the velocity profile are shown in figure 2(a) for slip flow with $Kn = 0.05$. The main feature is of course the finite velocity slip at the wall, $r = 1$, which is not zero. The correction of the zero-order solution due to the first- and second-order terms is very small, $< 10^{-5}$, and could justifiably be neglected in the computation of the normalized velocity profile. However, in this case the normalized velocity profile does vary with the streamwise location since the Knudsen number is a function of the pressure, which decreases from P_i to P_o. The slip flow effect on the normalized velocity profile is demonstrated in figure 2(b). As expected, the gas velocity at the wall increases with increasing Knudsen number.

The streamwise evolution of various flow parameters depends on the working gas, channel geometry and inlet/outlet conditions. An example for nitrogen gas as the working fluid in a microchannel $40\,\mu m \times 1\,\mu m \times 4000\,\mu m$ in dimensions, under a pressure ratio of 10, is depicted in figure 3. The density, centreline velocity and Mach number are plotted in figure 3(a) while the pressure and Knudsen number are plotted in figure 3(b), as a function of the downstream location from the channel inlet. The symbols are the results for no-slip flow, $Kn = 0$, while the curves are the results for the slip flow, $Kn_o = 0.06$. The slip-flow effect on the density and the pressure distribution is clearly negligible, as was reported by Arkilic et al. (1997).
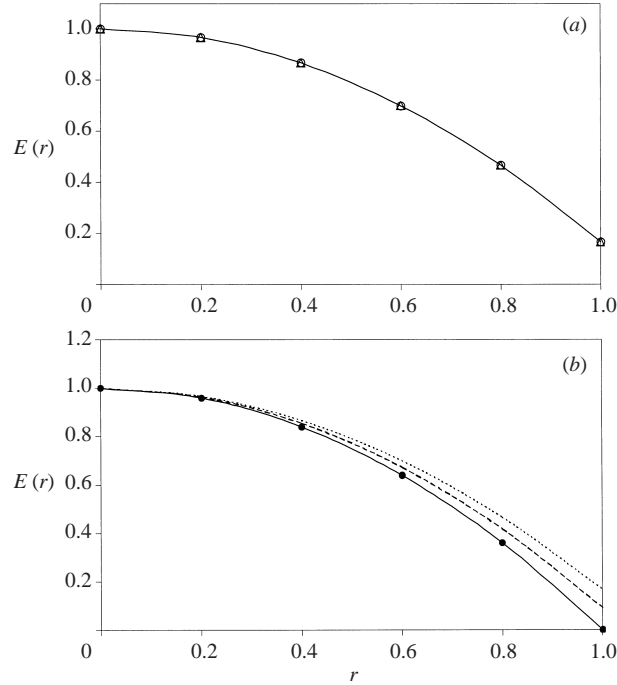
FIGURE 2. Slip-flow effect on the cross-stream velocity profiles. (*a*) $Kn = 0.05$: ——, $E^{(0)}(r)$; $\bigcirc$, $E^{(1)}(r)$; $\triangle$, $E^{(2)}(r)$; and (*b*) ——, $Kn = 0$; - - -, $Kn = 0.025$; $\cdots\cdots$, $Kn = 0.05$; ●, parabolic $(1 - r^2)$.

They suggested a simplified model to calculate the pressure distribution as follows:

$$\frac{P(x)}{P_o} = -6Kn_o + \left\{ \left(6Kn_o + \frac{P_i}{P_o} \right)^2 - \left[\left(\frac{P_i^2}{P_o^2} - 1 \right) + 12Kn_o \left(\frac{P_i}{P_o} - 1 \right) \right] \left(\frac{x}{L} \right) \right\}^{1/2},$$
(56)

and the agreement between calculations based on the two models is within 0.5%. The non-linear streamwise pressure distribution is the result of the compressible effect as the gas pressure decreases from the inlet to the outlet atmospheric pressure and, accordingly, the density also decreases. The Knudsen number, inversely proportional to the pressure, increases to its maximum value at the channel outlet.

The only parameter to be noticeably modified due to the slip-flow effect is the centreline velocity $u_c(x)$. Since the velocity at the wall is no longer zero and the pressure gradient is practically the same, the centreline velocity is higher compared with the no-slip flow, $Kn = 0$. It increases from a minimum value at the inlet to its maximum value at the outlet. Accordingly, the Mach number is also increasing along the channel to a maximum value of 0.025 at the channel outlet. All the parameters exhibit a rapid change close to the channel exit, $0.8 < \xi < 1.0$, compared to the slow variations along most of the channel, $0 < \xi < 0.8$, due to compressibility. Once the centreline velocity distribution along the channel is obtained, the entire velocity field $u(y, x)$ can be calculated. The velocity profiles at the inlet, mid-channel and outlet locations are plotted in figure 4 with and without the slip-flow effect.

The contribution of different effects to the resulting mass flow rate is demonstrated in figure 5, where the calculations are carried out for nitrogen with $P_o = 0.1\,\text{MPa}$.
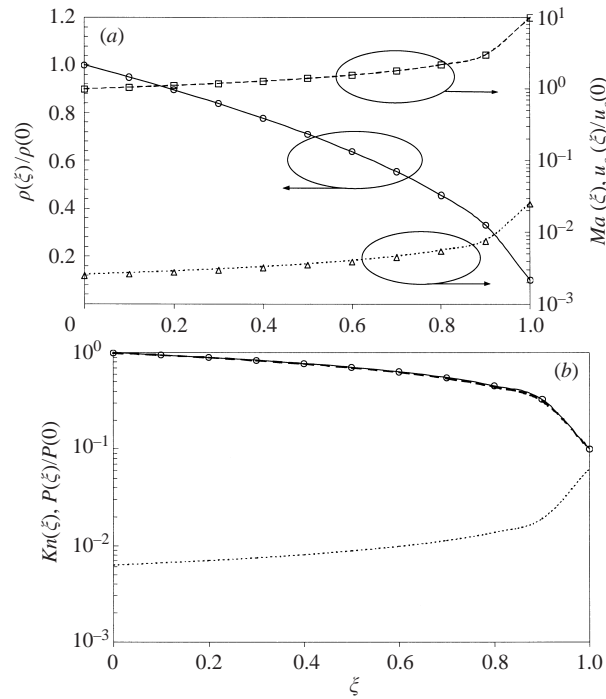
FIGURE 3. A comparison between slip (curves, $Kn > 0$) and no-slip (symbols, $Kn = 0$) streamwise distributions of: (a) –⊖–, density; --⊟--, centreline velocity; ..△.., Mach number; and (b) –⊖–, pressure; –––, equation (56), ·····, Kn.
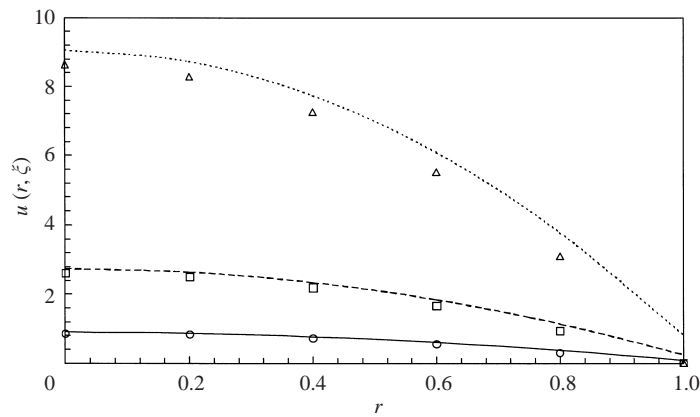

FIGURE 4. A comparison between slip (curves, $Kn > 0$) and no-slip (symbols, $Kn = 0$) cross-stream velocity distributions at: –⊖–, $\xi = 0$; --⊟--, $\xi = 0.9$; ..△.., $\xi = 1$.

Clearly, the most dramatic effect is due to compressibility when comparing the incompressible curve, Q_i, with the curve calculated with the compressibility effect only, $Q_i \alpha_C$. The only other significant effect is due to the slip flow, $Q_i \alpha_C (1 + \alpha_S)$, which increases the mass flow rate by about 10%. However, the correction of the compressible mass flow rate due to the acceleration and non-parabolic velocity profile, α_{AP}, is evidently negligible. The same simplified two-dimensional model as used for
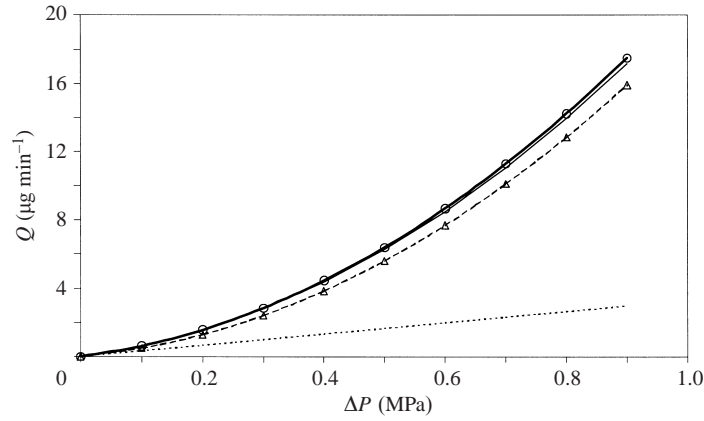
FIGURE 5. Mass flow rate dependence on the pressure drop accounting for slip, compressible, acceleration and non-parabolic velocity profile effects: $\cdots\cdots$, Q_i; $-----$, $Q_i\alpha_C$; $\triangle$, $Q_i\alpha_C(1+\alpha_{AP})$; $——$, $Q_i\alpha_C(1+\alpha_S)$; $\bigcirc$, $Q_i\alpha_C(1+\alpha_S)(1+\alpha_{AP})$; $——$, equation (57).

the derivation of equation (56), can be used to calculate the mass flow rate as follows:

$$Q = \frac{H^3 D P_o^2}{3RT\mu L}\left[\left(\frac{P_i}{P_o}\right)^2 - 1 + 12Kn_o\left(\frac{P_i}{P_o} - 1\right)\right]. \tag{57}$$

This model accounts only for the compressible- and slip-flow effects. Hence, the agreement between the current results and calculations based on equation (57) further confirms that the other effects can indeed be neglected.

5. Experimental arrangements

An experimental investigation of gas flows in straight and uniform microchannels was also conducted. The microdevices were designed for flow rate and pressure distribution measurements, utilizing standard micromachining techniques. Hence, each device included a single microchannel with integral pressure microsensors. The design parameters were selected based on the limitations of the fabrication technology and the constraints of the connection to the external fluid handling system.

5.1. Integral microchannel design

In surface microfabrication technology, using the sacrificial layer technique, it is difficult to deposit films thicker than $1\,\mu m$. On the other hand, the formation of a suspended membrane with a gap smaller than $0.5\,\mu m$ is limited by the stiction problem. Therefore, two nominal channel heights were chosen for this study, 0.5 and $1\,\mu m$, providing almost one order of magnitude difference in mass flow rate. The channel width should be as large as possible, not only to increase the mass flow rate, allowing more accurate measurements, but also to better approximate a two-dimensional flow field for comparison with analytical models. A width of $40\,\mu m$ was found to provide the maximum aspect ratio, at least 40, while avoiding the stiction problem.

The mass flow rate is inversely proportional to the channel length. Thus, for a given channel cross-section, it is desirable to minimize the channel length in order to maximize the mass flow rate. The microchannels were designed to be on the front side of the wafer and connected to the external fluid handling system from the back-side
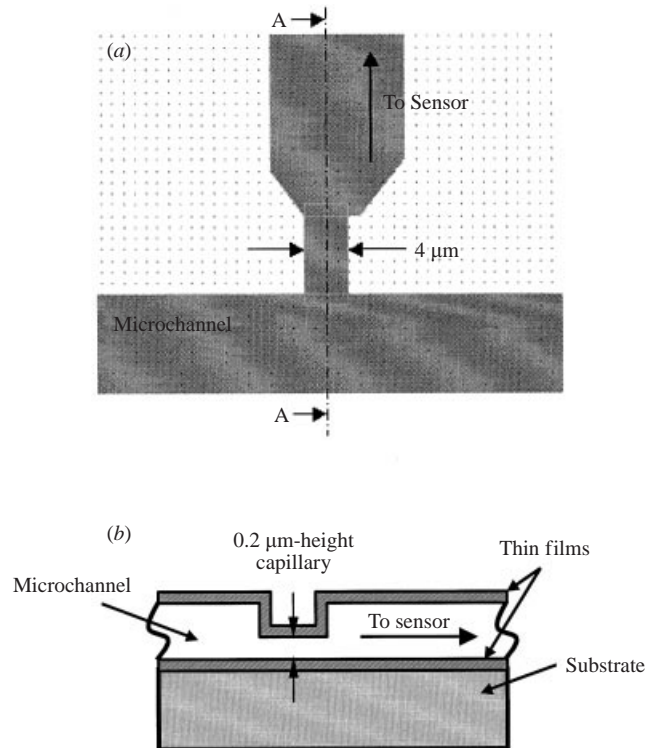
FIGURE 6. Schematic drawing of the capillary connecting the integrated pressure sensor to the microchannel: (*a*) top view, and (*b*) A-A cross-section (side view).

of the wafer. Therefore, holes through the wafers were required to allow the flow of gas in and out of the microchannel. Alignment and dead-volume considerations dictated an opening area of about $100\,\mu m^2$ to the channel at the substrate front side. The inlet/outlet holes were formed by wet etch, resulting in walls slanted at a $54.74°$ angle. Hence, each hole required an opening of approximately $800\,\mu m^2$ at the substrate back side. Each microchannel was linked to the external system via ceramic adaptors, having 1.5 mm inner diameter and 0.75 mm thick walls. Thus, the minimum channel length that could allow convenient connection of the microchannel devices to the external system was about 4 mm. Consequently, the nominal dimensions of the microchannels were determined to be $40\,\mu m$ in width, $4000\,\mu m$ in length, and either 0.5 or $1\,\mu m$ in height.

Pressure sensors were designed based on piezoresistive elements attached to a square membrane, such that any pressure difference across the membrane results in its deflection, consequently straining the piezoresistors and changing their resistance. Each sensor connection to the microchannel sidewall was designed as a capillary with the smallest possible cross-section area, as schematically shown in figure 6, to minimize its effect on the flow field. The local sacrificial layer thickness forming the capillary determines its final height. Therefore, the overall sacrificial layer was designed as a combination of two films: the first (either $0.3\,\mu m$ or $0.8\,\mu m$ thick) to define the microchannel and pressure sensor chambers, and the second (about $0.2\,\mu m$ thick) to define the capillary. Isotropic wet etch is used to pattern the sacrificial layer. Therefore, the minimum feature size in the mask layout should be at least $4\,\mu m$ to
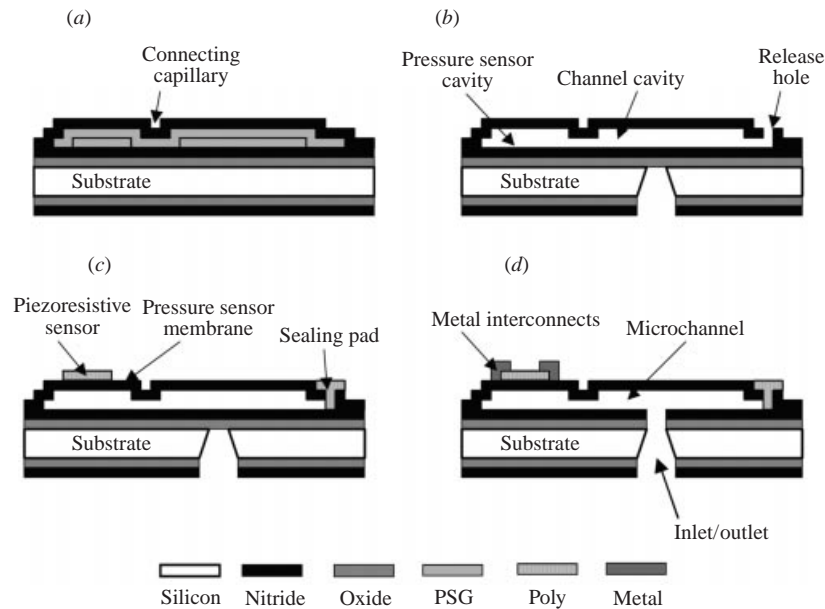
FIGURE 7. Schematic cross-sections of the major steps to fabricate the microchannels integrated with pressure microsensors.

ensure a consistent final feature size of 2 μm, since a feature size smaller than 2 μm might not survive the patterning process.

The sensor membrane area should be as large as possible to obtain maximum deflection, but a large membrane over a small gap could result in the stiction of the membrane to the underlying substrate. It was experimentally found that almost all the membranes survive if the area is not larger than 100 μm × 100 μm, with a gap up to 1 μm, while the sensitivity was still acceptable. Since the membrane deflection was expected to be very small, four piezoresistive sensing elements were designed in a Wheatstone bridge configuration to amplify the output signal. The bridge output-voltage change due to the resistance change, under constant bridge voltage, indicates the pressure difference across the sensor membrane.

5.2. *Microsystem fabrication and packaging*

Schematic cross-sections of the main fabrication steps are shown in figure 7. The fabrication started with the formation of a 0.15 μm thermal silicon dioxide film and a 0.3 μm thick low-stress silicon nitride film, for insulation, on an (100) oriented silicon wafer about 550 μm thick. This was followed by the deposition and patterning of a phosphosilicate glass (PSG) layer, either 0.3 μm or 0.8 μm in thickness, to form the channel and sensor chambers. Another 0.2 μm-thick PSG film was then deposited and patterned for the small capillaries, connecting the sensors to the channels, and etching holes. Next, a structural layer of low-stress silicon nitride, 1 to 2 μm in thickness, was deposited to form the channel sidewalls and ceiling as well as the sensor membranes, figure 7(a). Orientation-dependent TMAH wet etching was used to create the inlet/outlet holes from the wafer back side, utilizing the oxide/nitride insulating stacked layer as an etch mask. The TMAH etch stopped at the insulating layer on the wafer front side. Following the opening of the etching holes on the nitride structural layer, the PSG sacrificial layer was etched by 49% hydrofluoric
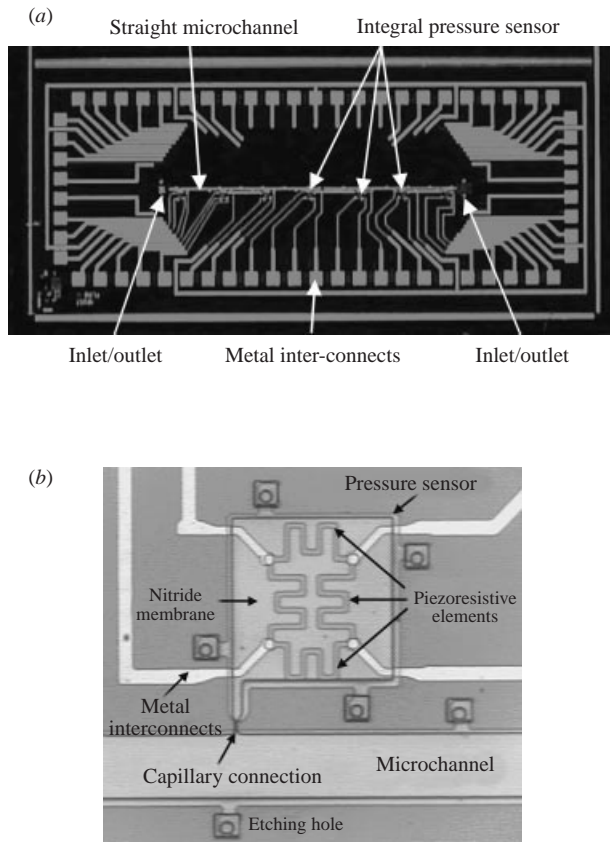
FIGURE 8. Pictures of: (*a*) a fabricated device, showing the microchannel, pressure sensors, channel inlet/outlet and metal interconnects; and (*b*) a close-up of the pressure sensor, with the capillary connection to the microchannel.

acid (HF), figure 7(*b*). This step is very critical since concentrated HF also etches silicon nitride. Since the time to complete the removal of the PSG layer could not be long, the distance between adjacent etching holes should be designed properly. In the present work, the distance was about 150 µm, resulting in a release time of approximately 10 min. The exposed inner surfaces of the microchannels, after the sacrificial-layer etch, were silicon nitride films with surface roughness of about 15 nm. A polycrystalline silicon layer of 0.5 µm in thickness was then deposited, boron doped and patterned for both piezoresistor formation and etching-hole sealing, figure 7(*c*). A 1 µm thick aluminium layer for interconnections was next sputter deposited, patterned and sintered. Finally, the fabrication process was completed with the etching of the films separating the microchannels from the inlet/outlet holes, figure 7(*d*). Pictures of an overview of a fabricated microdevice and a close-up of an integrated pressure sensor are depicted in figure 8.

The height of the microchannel is dictated by the thickness of the sacrificial layer; although the thickness cannot be controlled precisely due to random variables in the deposition process, it can be measured accurately. However, during the sacrificial-layer etch for the channel formation, the nitride inner surfaces were also slightly etched. This resulted in a channel height larger than the sacrificial-layer thickness. A few fabricated samples were cut to take scanning electron microscopy (SEM)
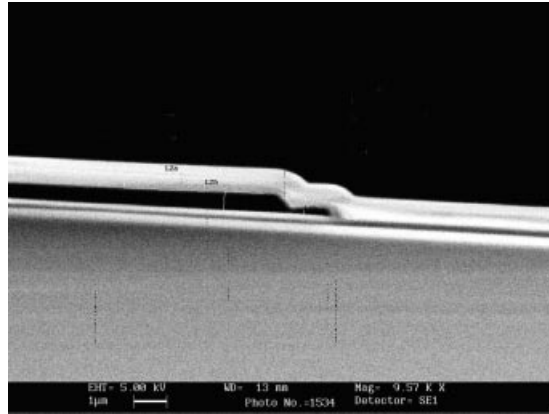
FIGURE 9. A SEM picture of a microchannel cross-section showing the channel height to be about 0.53 µm after completing the device fabrication.
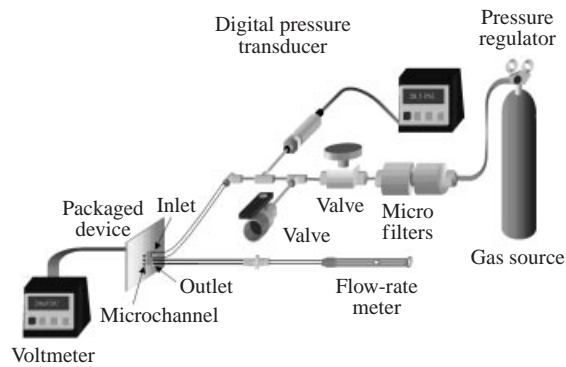

FIGURE 10. A schematic illustration of the experimental set-up.

micrographs of the cross-sections, as in the example shown in figure 9, in order to determine the channel height as precisely as possible. The SEM cross-sections revealed that the actual height of the microchannels was either 0.53 µm or 0.97 µm compared to the design values of 0.5 µm and 1.0 µm, respectively. Test microchannels that were fabricated near microchannels used for the SEM pictures, on the same wafer, were assumed to have similar height.

The processed wafers were diced into individual dies. Upon inspection, dies that survived the fabrication process were glued to custom-made lead-frames and, subsequently, wire-bonded to enable input/output of electrical signals to/from the sensors.

5.3. *Experimental set-up*

A schematic diagram of the experimental set up is given in figure 10. Three different gases were used for the flow rate measurements: nitrogen, argon and helium. Each gas was supplied from a separate high-pressure gas cylinder, at 10 MPa minimum, and the flow rate was adjusted utilizing a two-stage pressure regulator. The working gas was first passed through filters to prevent channel clogging, and then was forced through the microchannel under inlet gauge pressure of up to 400 kPa. A pressure transducer, Druck pressure calibrator model DPI 602 with accuracy of 0.01% full scale of up to 2 MPa, was located at the channel inlet to measure the driving pressure drop, while a voltmeter was connected to the integrated pressure sensors on the packaged

	Helium	Argon	Nitrogen
Density, ρ [kg m^{-3}]	0.17	1.69	1.19
Specific constant, R [kJ kg^{-1} K^{-1}]	2.077	0.20813	0.2968
Viscosity, μ [kg m^{-1} s^{-1}]	1.99×10^{-5}	2.27×10^{-5}	1.79×10^{-5}
Mean free path, λ [μm]	0.20377	0.10396	0.0628

TABLE 1. Gas properties at ambient conditions of $T_a = 293$ K and $P_a = 1$ atm.

microdevice to measure the pressure distributions along the channel. The driving pressure drop was kept below 1 MPa, not only to ensure subsonic flow along the entire microchannel, but also to avoid the frequent failure of the connection between the external fluid handling system and the packaged device at higher inlet pressure.

The flow rate was measured using a 10 μl glass syringe opened to the ambient pressure. The volume flow rate was determined visually as a meniscus of water travelled past the marked scale on the syringe as a function of time. Multiplying this rate by the outlet gas density, under ambient conditions, yields the mass flow rate. The pressure loss required to move the meniscus of water in the syringe, about 0.5 kPa, is negligible due to the significant total pressure drop across the microchannel (at least 100 kPa). Since the pressure upstream and downstream of the water meniscus is almost identical, diffusion of the working gas through the meniscus can be neglected. For sensor calibration, both the inlet and outlet of the microchannel were connected to the gas source, ensuring uniform static pressure throughout the entire microsystem, and the pressure was adjusted using the transducer. Once a steady state was reached, the voltage output of all sensors was recorded. The process was repeated 6–8 times to obtain a calibration curve for each sensor.

6. Mass flow rate measurements

In the slip flow regime, $0.001 < Kn < 0.1$, the no-slip boundary condition is no longer valid. Although the interaction between the gas molecules and the solid boundary (the accommodation coefficient) is a function of both gas properties and boundary surface, most engineering surfaces have near unity values of full accommodation (Arkilic *et al.* 1997). Indeed, the surface roughness in the present devices is about 15 nm, almost two orders of magnitude larger that the gas molecular diameter. This most probably would result in a diffuse reflection boundary condition, namely full accommodation of the streamwise momentum. The resulting velocity slip at the wall is then directly proportional to the Knudsen number. Therefore, three different gases were used as working fluids: two monatomic noble gases, helium and argon, and one diatomic inert gas, nitrogen. The mean free path of helium is double that of argon, enhancing the slip flow effect. The three tested gases are commercially available at electronic grade, with purity better than 99.9%, such that the presence of other gases can be neglected, and their physical properties are listed in table 1.

Mass flow rate measurements were conducted for the three gases in both forward and backward directions to ensure that the channel was indeed symmetric with respect to the channel inlet and outlet, and no particles were trapped within the microsystem affecting the results. The difference between the inlet, P_i, and outlet pressure, P_o, was kept in the range 100–400 kPa. The experimental results are summarized in figure 11 as symbols. Under the same pressure drop, $\Delta P = P_i - P_o$, the argon flow rate is higher than the nitrogen flow rate, which in turn is higher than the helium flow rate,
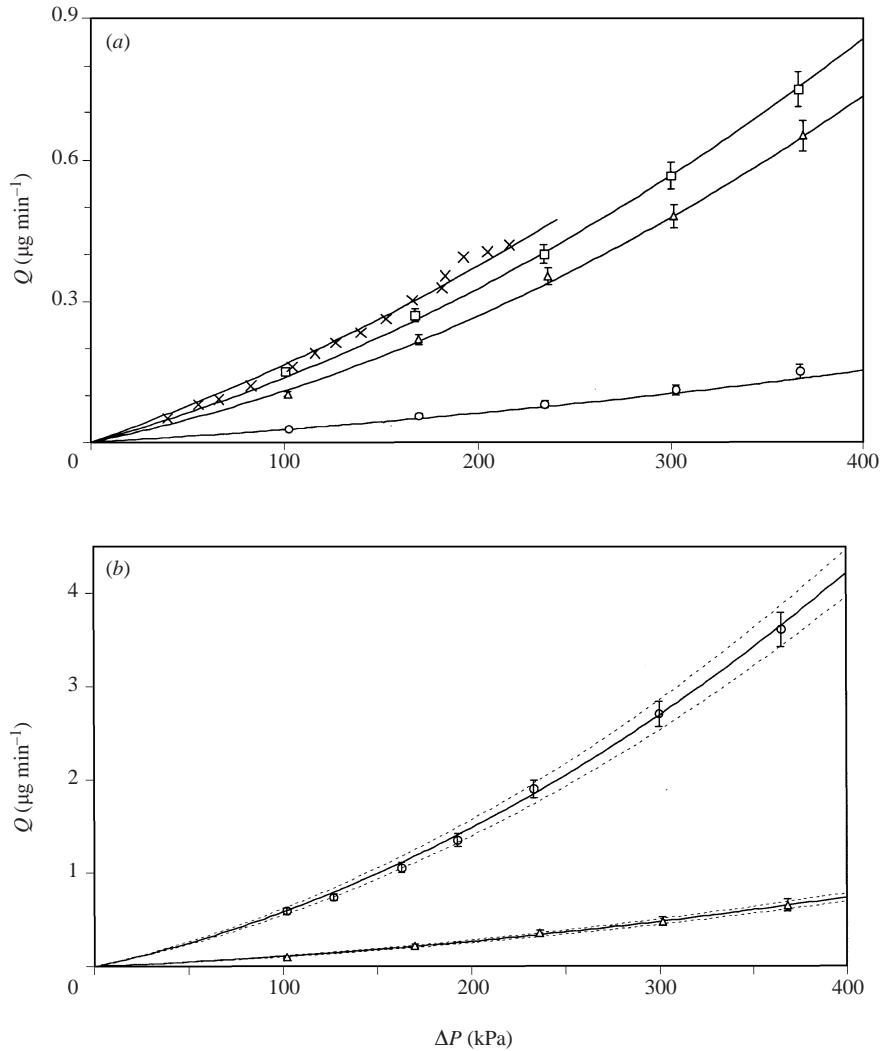
FIGURE 11. A comparison between measured (symbols) and calculated (curves) mass flow rate. (a) $2H = 0.53\,\mu\text{m}$; $\square$, argon; $\triangle$, nitrogen; $\bigcirc$, helium; $\times$, Shih *et al.* (1996). (b) Nitrogen: $\bigcirc$, $2H = 0.97\,\mu\text{m}$; $\triangle$, $2H = 0.53\,\mu\text{m}$ (solid lines are nominal flow rates; and dashed lines represent $\pm 6\%$ of the nominal rates).

figure 11(*a*). For comparison, helium flow measurements in a microchannel by Shih *et al.* (1996) are also included. The differences in the mass flow rate are mainly due to the gas density, since the mean free path and viscosity of the three gases are of the same order of magnitude. The strong dependence of the mass flow rate on the channel height is demonstrated in figure 11(*b*) for nitrogen flow.

In order to evaluate the slip-flow effect, the experimental results are compared with analytical predictions based on the derived theoretical model. It has been demonstrated that only the compressibility and slip-flow effects are important, while the flow acceleration and the non-parabolic velocity profile can be neglected. Therefore, the mass flow rate is calculated as follows:

$$Q = \frac{2}{3}\frac{DH^3}{\mu L}\Delta P\frac{P_o}{RT}\left(\frac{P_i + P_o}{2P_o}\right)(1 + 6Kn). \tag{58}$$

Mass flow rate calculations based on equation (58) are plotted in figure 11 as solid curves. The good agreement between the analytical and experimental results not only supports the basic assumptions made in deriving the theoretical model, but also confirms that accounting for compressibility and slip-flow effects only is sufficient to obtain correct mass flow rate predictions. Furthermore, the agreement between the two sets of experiments confirms that the experimental procedures are sound and the measurements can be repeated.

6.1. *Error analysis*

The theoretical model can also be used to evaluate the experimental error as every measured variable in equation (58) contributes to the overall uncertainty in the measured values of the mass flow rate. In order to simplify the analysis, the Knudsen number effect is neglected as it was found to be relatively small. Hence, the mass flow rate dependence on experimentally measured parameters is given by a simple expression:

$$Q \propto \frac{DH^3}{\mu L} \Delta P \frac{\overline{P}}{RT}, \tag{59}$$

where $\overline{P} = (P_i + P_o)/2$ is the mean pressure in the microchannel. Assuming the viscosity and specific gas constant are known to very high accuracy, standard error analysis then suggests the following relationship:

$$\frac{\delta Q_0}{Q_0} = \sqrt{9\left(\frac{\delta H_0}{H_0}\right)^2 + \left(\frac{\delta D_0}{D_0}\right)^2 + \left(\frac{\delta L_0}{L_0}\right)^2 + \left(\frac{\delta T_0}{T_0}\right)^2 + \left(\frac{\delta \Delta P_0}{\Delta P_0}\right)^2 + \left(\frac{\delta \overline{P}_0}{\overline{P}_0}\right)^2}$$

(60)

where the subscript 0 indicated nominally measured values, and δ indicates the experimental error of the measured parameter. Some of the errors, i.e. geometrical parameters, are systematic, while others, i.e. pressure and temperature, are random. In this case, the systematic errors would smoothly shift the entire curve of mass flow rate as a function of the pressure drop up or down, since the relative error is the same for all the measurements. On the other hand, random errors would result in fluctuations of data points within the same curve, since the error magnitude could vary from one experiment to the other.

Equation (60) clearly indicates that the most critical measured parameter dominating the experimental error is the height of the microchannel and, unfortunately, this is also the most difficult dimension to measure with high accuracy. However, the error in determining the exact height of the channel is systematic, and will be treated separately. In order to estimate the error in the measured mass flow rate due to all other parameters, the separate relative errors need to be evaluated. The microchannel width and length are measured optically with accuracy better than $0.5\,\mu\text{m}$ and $10\,\mu\text{m}$, respectively, resulting in approximately $\delta D_0/D_0 \approx \delta L_0/L_0 \sim 1\%$. The temperature is measured to within $1\,\text{K}$ leading to $\delta T_0/T_0 < 1\%$. Both the mean pressure and the pressure drop are determined from the inlet and outlet pressure measurements carried out by the same transducers with a relative error better than 1%. Therefore, setting aside the channel height uncertainty, the mass flow rate can be predicted by equation (58) to be within $\pm 2.5\%$. This is also the estimated spread in statistically independent direct measurements of the mass flow rate, i.e. repeating the measurements by duplicating the same conditions on different days by different users. Repeated mass flow rate measurements, while maintaining all other experimental parameters constant, are within 1%.

The cubic dependence of the mass flow rate on the microchannel height makes it vital to determine this parameter as accurately as possible. Measurements of the sacrificial layer thickness, though very accurate, are not adequate due to the etching of the structural layers during the sacrificial layer etch. Cutting the device and directly measuring the height at the end of the fabrication, as shown in figure 9, would provide a very accurate value. However, this is a destructive method since the device can no longer be used. Another approach is to cut a sample device for height measurements, and assume that the height of all channels on the same wafer is the same as that of the sample channel. We found that, in our lab, the height uniformity along a 4 mm long channel is about 1%, while the uniformity among channels across a 100 mm diameter wafer is about 5%. Therefore, as long as the test microchannel is located within 10 mm of the sample channel, the test channel height should be within 2% of the sample channel measured height. The 2% height uncertainty would result in an error of 6% in the mass flow rate. Experimental measurements (symbols) of nitrogen flow rate through two channels with different heights are compared with calculations (solid lines) and curves corresponding to $\pm 6\%$ of the theoretical values (dashed lines) in figure 11(*b*). To emphasize the importance of the channel height, the 6% difference between the design value of 0.5 μm and the actual value of 0.53 μm would result in 18% error in the mass flow rate, far greater than the error due to all other sources.

In fact, it is not the height of the fabricated microchannel that is important but rather the actual height during experimentation when the microchannel is pressurized. The channel bottom is deposited on the 0.55 mm thick silicon substrate, which is expected to remain flat during the experiments, even at high pressure. However, the microchannel cover is a silicon nitride membrane about 1–2 μm in thickness that can be deflected under high pressure. Wu *et al.* (1998) studied in detail this phenomenon, which was termed the bulging effect, and derived a simple model to account for it. They reported that a deviation of the measured mass flow rate from the theoretical prediction could be observed only for driving pressure higher than 1 MPa. Hence, the driving pressure in the current experiments was restricted to less than 0.5 MPa so that effect of the top-surface deflection on the channel height can be neglected.

Another major source of experimental error, which cannot be quantified, is leakage. Presumably, given the many connections and fittings between the gas reservoir and the test microchannel, there can be no absolutely leak-proof system. The quick leak check is carried out by immersing the entire pressurized system under water and, subsequently, looking for gas bubbles formed in the water. A more laborious and reliable technique is to connect the channel inlet and outlet to a common gas source at the highest possible pressure. If there is no leak, the pressure will hold steady. If there is a leak, the pressure will decrease with time.

7. Streamwise pressure distribution

It would be ideal to directly measure the velocity profiles in order to critically test theoretical models, since the mass flow rate presents only an integral parameter with no details of the flow field. However, at present, there is no known technique capable of measuring velocity profiles in sub-micron channels. The next best criterion is the pressure distribution. It is extremely difficult to measure the static pressure at more than a single point at a given cross-section, and previous studies support the assumption that the pressure can be considered uniform in a cross-section perpendicular to the flow direction (Harley *et al.* 1995). Therefore, the static pressure is measured at seven locations separated by a distance of about 650 μm.
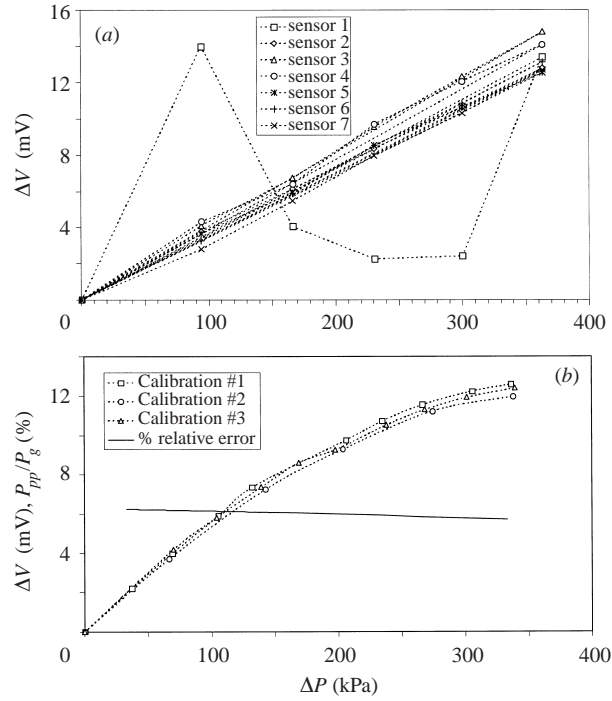
FIGURE 12. Pressure sensor calibration curves of voltage output dependence on the gauge pressure: (*a*) all sensors in a 0.53 μm high device, and (*b*) repeated calibrations of a single sensor with the normalized peak-to-peak pressure fluctuations in a 0.97 μm high device.

All pressure sensors were calibrated prior to the pressure distribution measurements, and the calibration curves are plotted in figure 12. The sensor sensitivity was on the average about $0.02\,\mathrm{mV\,kPa^{-1}\,V^{-1}}$, sufficient for the pressure range tested in this work. Unfortunately, the pressure sensors did not all always function properly as indicated in figure 12(*a*), where the output of one of the seven sensors is erratic. In many instances, this is the result of intermittent electrical contacts. In order to estimate the experimental error in the pressure measurements, the calibration process was repeated several times as demonstrated in figure 12(*b*). The output voltage from each sensor is converted to pressure using the corresponding calibration curve. Therefore, the accuracy of the pressure measurements is directly determined by the accuracy of the calibration curves. Different users repeated the calibration process independently on different days. For most sensors, the peak-to-peak pressure fluctuations, P_{pp}, are typically about 6% of the average pressure across the membrane, P_g, i.e. a relative experimental error of $\pm 3\%$. However, fluctuations up to $\pm 5\%$ were observed for the worst sensor, which can be regarded as a conservative estimate.

Pressure measurements were conducted using argon through the 0.53 μm high channel, and nitrogen through the 0.97 μm high channel; the data are summarized in figures 13(*a*) and 13(*b*), respectively. Only Shih *et al.* (1996) have reported similar measurements, and their results for helium flow in a microchannel are included for comparison. Pressure distributions were also calculated based on the theoretical model, equation (52) as follows:

$$P(\xi) = RT \left[\varphi_0(\xi) + \frac{B1}{RT} \ln \frac{\varphi_0(\xi)}{\rho_o^2} - \frac{C1}{(RT)^3} \frac{6A1^2}{\rho_o^2} \frac{1-\xi}{\varphi_0(\xi)} \right]^{1/2}. \qquad (61)$$
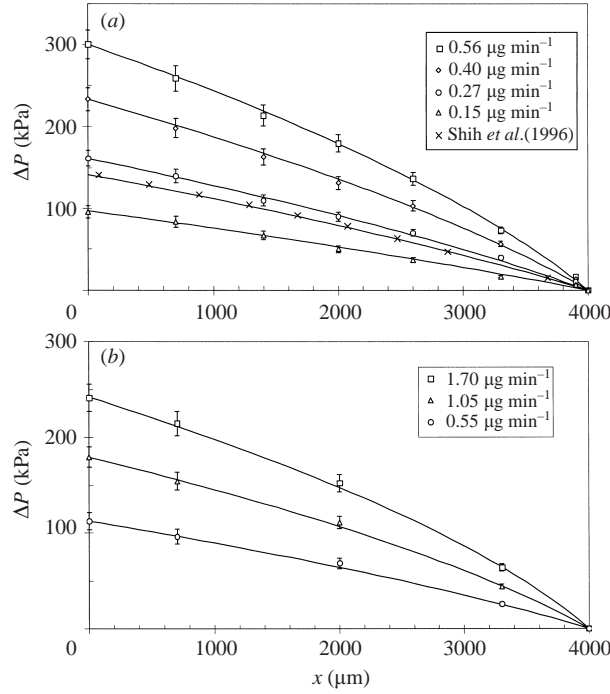
FIGURE 13. A comparison between measured (symbols) and calculated (curves) streamwise pressure distributions for: (*a*) argon in the 0.53 μm high microchannel, and (*b*) nitrogen in the 0.97 μm high microchannel, for different mass flow rates.

The constants $A1$, $B1$ and $C1$ are calculated based on equation (46), while the function $\varphi_0(\xi)$ is given by

$$\varphi_0(\xi) = \rho_o^2 - \frac{2A1}{RT}(1 - \xi). \tag{62}$$

The calculated curves for all the test conditions are compared with the measurements in figure 13, where the agreement between the experimental and analytical results is well within the experimental error. The nonlinear pressure distribution due to the compressible effect is evident, as reported previously (Shih *et al.* 1996). The results confirm that the molecular structure, i.e. monatomic or diatomic, has no effect on the flow field. Furthermore, the good agreement demonstrated in figure 13 also suggests that the capillaries connecting the pressure sensors to the microchannel sidewall had a negligible effect on the flow development.

8. Conclusions

An analytical solution to calculate the flow field of a steady isothermal compressible laminar gas flow in either a circular or a planar microchannel has been derived using a perturbation expansion method. The theoretical approach, accounting for compressibility, slip, acceleration and non-parabolic velocity profile effects, allows the explicit derivation of the cross-stream and the streamwise dependence of flow parameters without the need for numerical simulations. Compressibility is found to have the most dominant zero-order effect on the flow development. The pressure distribution is nonlinear and the mass flow rate more than doubles compared with an incompressible flow under the same pressure drop. The slip-flow effect also enters the solution explicitly as a zero-order correction through the velocity-slip boundary

condition. Hence, it is mainly manifested in the modified velocity profiles and, consequently, it results in an enhanced mass flow rate. However, the pressure gradient with or without the slip-flow effect is about the same. The combined effect of flow acceleration and non-parabolic velocity profile is a first-order correction and can be neglected.

A microsystem comprising a microchannel flow cell, less than 1 μm in height, with integral pressure microsensors has been fabricated and tested. Mass flow rate and pressure distribution measurements were conducted using argon, nitrogen and helium as the working gases under inlet gauge pressure up to 0.5 MPa. An uncertainty analysis revealed that the most critical experimental parameter is the channel height, especially for the flow rate, which is a cubic function of the height. Accounting for other sources of error, with the current technology, it is possible to obtain mass flow rate and pressure measurements with a $\pm 3\%$ relative error. However, a $\pm 3\%$ uncertainty in the channel height means a $\pm 9\%$ uncertainty in mass flow rate measurements; thus, overwhelming all other errors. Determining the channel height accurately could be a major challenge and destructive methods may be required. The agreement between the experimental and analytical results confirms that compressibility and velocity slip are the dominant effects in subsonic gas flows in the slip flow regime.

REFERENCES

ARKILIC, E. B., SCHMIDT, M. A. & BREUER, K. S. 1997 Gaseous slip flow in long microchannels. *J. Microelectromech. Syst.* **6**, 167–178.

VAN DEN BERG, H. R., TEN SELDAM, C. A. & VAN DER GULIK, P. S. 1993a Compressible laminar flow in a capillary. *J. Fluid Mech.* **246**, 1–20.

VAN DEN BERG, H. R., TEN SELDAM, C. A. & VAN DER GULIK, P. S. 1993b Thermal effects in compressible viscous flow in a capillary. *Intl J. Thermophys.* **14**, 865–892.

BESKOK, A. & KARNIADAKIS, G. E. 1994 Simulation of heat and momentum transfer in complex microgeometries. *J. Thermophys. Heat Transfer* **8**, 647–655.

BESKOK, A., KARNIADAKIS, G. E. & TRIMMER, W. 1996 Rarefaction and compressibility effects in gas microflows. *Trans. ASME: J. Fluids Engng* **118**, 448–456.

CERCIGNANI, C., ILLNER, R. & PULVIRENTI, M. 1994 *The Mathematical Theory of Dilute Gases.* Springer.

CHOI, S. B., BARRON, R. F. & WARRINGTON, R. O. 1991 Fluid flow and heat transfer in microtubes. *ASME DSC* **32**, 123–134.

CHU, R. K.-H. & ZOHAR, Y. 2000 A class of discrete kinetic solutions for non-boundary-driven gas flow. *J. Non-Equilib. Thermodyn.* **25**, 49–62.

HARLEY, J. C., HUANG, Y., BAU, H. H. & ZEMEL, J. N. 1995 Gas flow in micro-channels. *J. Fluid Mech.* **284**, 257–274.

HO, C. M. & TAI, Y. C. 1996 MEMS and its applications for flow control. *Trans. ASME: J. Fluids Engng* **118**, 437–447.

HO, C. M. & TAI, Y. C. 1998 Micro-electro-mechanical systems (MEMS) and fluid flows. *Annu. Rev. Fluid Mech.* **30**, 579–612.

HUNTER, R. J. 1981 *Tzeta Potential in Colliod Science: Principles and applications.* Academic.

JIANG, L., WANG, Y., WONG, M. & ZOHAR, Y. 1999 Fabrication and characterization of a microsystem for a microscale heat transfer study. *J. Micromech. Microengng* **9**, 422–428.

LEE, S. Y. K., WONG, M. & ZOHAR, Y. 2001 Gas flow in microchannels with bends. *J. Micromech. Microengng* **11**, 635–644.

LEE, W. Y., WONG, M. & ZOHAR, Y. 2002a Microchannels in series connected via a contraction/expansion section. *J. Fluid Mech.* **459**, 187–206.

LEE, W. Y., WONG, M. & ZOHAR, Y. 2002b Pressure loss in constriction microchannels. *J. Microelectromech. Syst.* **11**, 236–244.

LIU, J. Q., TAI, Y. C., PONG, K. C. & HO, C. M. 1993 Micromachined channel/pressure sensor systems for micro flow studies. *Proc. 7th Intl Conf. Solid-State Sensors and Actuators, Transducers'93*, pp. 995–999.

MEINHART, C. D., WERELEY, S. T. & SANTIAGO, J. G. 1999 PIV measurements of a microchannel flow. *Exps. Fluids* **27**, 414–419.

PFAHLER, J., HARLEY, J. C., BAU, H. & ZEMEL, J. N. 1991 Gas and liquid flow in small channels. *ASME DSC* **32**, 49–60.

PIEKOS, E. S. & BREUER, K. S. 1996 Numerical modeling of micromechanical devices using the direct simulation Monte Carlo method. *Trans. ASME: J. Fluids Engng* **118**, 464–469.

PONG, K. C., HO, C. M., LIU, J. Q. & TAI, Y. C. 1994 Non-linear pressure distribution in uniform microchannels. *ASME FED*, vol. 197, pp. 51–56.

PRUD'HOMME, R. K., CHAPMAN, T. W. & BOWEN, J. R. 1986 Laminar compressible flow in a tube. *Appl. Sci. Res.* **43**, 67–74.

SCHAAF, S. A. & CHAMBRE, P. L. 1961 *Flow of Rarefied Gases*. Princeton University Press.

SHIH, J. C., HO, C. M., LIU, J. Q. & TAI, Y. C. 1996 Monatomic and polyatomic gas flow through uniform microchannels. *ASME DSC* **59**, 197–203.

SREEKANTH, A. K. 1968 Slip flow through long circular tubes. In *Rarefied Gas Dynamics* (ed. L. Trilling & H. Y. Wchman). Academic.

STOKES, V. K. 1984 *Theories of Fluids with Microstructure*. Springer.

WU, P. & LITTLE, W. A. 1983 Measurements of friction factors for the flow of gases in very fine channels used for microminiature Joule–Thomson refrigerators. *Cryogenics* **23**, 273–277.

WU, S., MAI, J., ZOHAR, Y., TAI, Y. C. & HO, C. M. 1998 A suspended microchannel with integrated temperature sensors for high-pressure flow studies. *Proc. 11th IEEE Workshop on Micro Electro Mechanical Systems, MEMS'98*, pp. 87–92.